

Bayesian Framework for the $E1$ and $E2$ Astrophysical Factors at 300 keV from Subthreshold and Ground-State Asymptotic Normalization Coefficients

A. M. Mukhamedzhanov¹

¹*Texas A&M University, College Station, TX 77843, USA*

The $^{12}\text{C}(\alpha, \gamma)^{16}\text{O}$ reaction governs the carbon-to-oxygen ratio set during helium burning, shaping white-dwarf structure and Type Ia supernova yields. At the astrophysical energy $E \approx 300$ keV, the cross section is controlled by the subthreshold 1^- (7.12 MeV) and 2^+ (6.92 MeV) states, whose contributions depend on their asymptotic normalization coefficients (ANCs) C_1 and C_2 , respectively. We perform a Bayesian analysis of the $S_{E1}(300 \text{ keV})$ and $S_{E2}(300 \text{ keV})$ factors using calibrated R -matrix mappings and experimental ANC constraints for the 1^- , 2^+ , and 0^+ ground state. For $S_{E1}(300 \text{ keV})$, flat prior on the 1^- ANC lead to broad posterior with 68% credible interval spanning [71.4, 93.4] keV b, while Gaussian priors concentrate weight near the reported ANC values and yield narrower posteriors. For $S_{E2}(300 \text{ keV})$, the analysis includes the interference of the radiative transition through the subthreshold resonance with the direct capture to the ground-state, which depends on the ground-state ANC C_0 , giving broad posterior with 68% credible interval spanning [30.7, 50.5] keV b. The Gaussian priors centered near anchor values. The resulting posteriors quantify both correlations and uncertainties: despite incorporating the published ANC constraints, the 68% intervals remain broad, showing that present ANC determinations do not yet reduce the astrophysical uncertainty. Overall, the Bayesian framework provides statistically robust posteriors for $S_{E1}(300 \text{ keV})$ and $S_{E2}(300 \text{ keV})$, improving the reliability of extrapolations for stellar modeling and nucleosynthesis.

I. INTRODUCTION

The $^{12}\text{C}(\alpha, \gamma)^{16}\text{O}$ reaction is one of the most important processes in nuclear astrophysics. Together with the triple- α process, it governs the carbon-to-oxygen ratio established at the end of helium burning in red giant stars. This ratio strongly influences subsequent stellar evolution, the structure of white dwarfs, and the nucleosynthetic yields of Type Ia supernovae. Precise knowledge of the low-energy S -factor is therefore essential for stellar modeling. The relevant energies lie near $E \approx 300$ keV, deep in the sub-Coulomb region, where direct cross-section measurements are extremely challenging due to the vanishingly small reaction rate.

At these low energies, the S -factor is dominated by radiative capture through two near-threshold subthreshold states of ^{16}O : the 1^- state at 7.12 MeV and the 2^+ state at 6.92 MeV. These states, lying just below the $\alpha + ^{12}\text{C}$ threshold, contribute disproportionately to the capture probability through the extended tails of their bound-state wave functions in the external region. Their contributions to the $E1$ and $E2$ components of the S -factor are determined by the overlap between the scattering wave function and the asymptotic bound-state tails. This overlap is quantified by the asymptotic normalization coefficients (ANCs), which thus provide the key nuclear-structure input for extrapolating the S -factor into the astrophysical Gamow window. Accurate determination of the ANCs for the 1^- and 2^+ states, as well as for the ^{16}O ground state, remains central to reducing the large uncertainties in S_{E1} and S_{E2} [1].

A detailed analysis of the role of these ANCs was presented in Ref. [1], where the contributions of the subthreshold states to the total S -factor at 300 keV were estimated to be 71–74% for $E1$ and 102–103% for $E2$

at low ground-state ANC, respectively. That study also identified correlations between the uncertainties in the subthreshold ANCs and the extrapolated S_{E1} and S_{E2} factors. After decades of experimental and theoretical work, the values of the 1^- and 2^+ ANCs have been constrained to the intervals summarized in Table I.

In light of these advances, Bayesian statistical methods provide a systematic framework to address the remaining uncertainties. Within the R -matrix description, Bayesian inference combines prior information on ANCs (from transfer reactions, elastic scattering, or theoretical models) with likelihoods based on capture and scattering data. This approach yields full posterior probability distributions for the ANCs and, consequently, for the extrapolated S -factors. Unlike traditional fits that return only central values and approximate error bars, the Bayesian framework quantifies correlations, propagates uncertainties consistently, and provides well-defined credible intervals (CIs) for S_{E1} and S_{E2} . Such probabilistic treatments have been applied, for example, in recent Bayesian R -matrix analyses [2]. In the present work, we extend this approach by explicitly incorporating the existing ANC constraints for the 1^- and 2^+ subthreshold states and the 0^+ ground state of ^{16}O , thereby producing statistically robust posteriors for the astrophysical S -factors at 300 keV. In what follows, we simplify notation by writing $S_{Ei} \equiv S_{Ei}(300 \text{ keV})$, $i = 1, 2$, so that S_{E1} and S_{E2} denote the astrophysical S -factors evaluated at $E = 300$ keV. Captions, tables and section titles retain the explicit 300 keV label for clarity.

II. STATE OF KNOWLEDGE OF SUBTHRESHOLD (1^- AND 2^+) AND GROUND-STATE ANCS

Table I summarizes the most reliable determinations of the ANCs for the $^{16}\text{O}^* \rightarrow \alpha + ^{12}\text{C}$ channels, derived from transfer reactions, elastic scattering extrapolations, and theoretical analyses.

TABLE I. ANC values C_ℓ ($\text{fm}^{-1/2}$) for $^{16}\text{O}^*(J^\pi) \rightarrow \alpha + ^{12}\text{C}(\text{g.s.})$.

$C_0; J^\pi = 0^+$	$C_2; J^\pi = 2^+$	$C_1; J^\pi = 1^-$	References
(139 \pm 8)	$(1.11 \pm 0.10) \times 10^5$	$(2.08 \pm 0.19) \times 10^{14}$	[3]
	$(1.22 \pm 0.06) \times 10^5$	$(2.10 \pm 0.14) \times 10^{14}$	[4]
	$(0.98 \pm 0.08) \times 10^5$	$(1.83 \pm 0.08) \times 10^{14}$	[5]
	$(1.40 \pm 0.42) \times 10^5$	$(1.87 \pm 0.32) \times 10^{14}$	[6]
	$(1.44 \pm 0.26) \times 10^5$	$(2.00 \pm 0.69) \times 10^{14}$	[7]
58	$(1.07 \pm 0.06) \times 10^5$	$(1.85 \pm 0.07) \times 10^{14}$	[4, 5]
	$(1.10 - 1.31) \times 10^5$	$(2.21 \pm 0.07) \times 10^{14}$	[8]
	1.14×10^5	2.08×10^{14}	[9]
	$(1.42 \pm 0.05) \times 10^5$	$(2.27 \pm 0.02) \times 10^{14}$	[10]
(337 \pm 45)			[11]
709			[12]
740			[13]
(637 \pm 86)			[14]
(744 \pm 144)			[15]

Following Ref. [5], the ANCs of Refs. [3, 4] have been renormalized to $C_1 = 1.83 \times 10^{14} \text{ fm}^{-1/2}$ and $C_2 = 0.98 \times 10^5 \text{ fm}^{-1/2}$, which we adopt as the lower bounds of our prior intervals, while the R -matrix anchors are taken from Ref. [1].

A. ANC C_1

The subthreshold 1^- ANC lies in the range $C_1 = (1.83 - 2.27) \times 10^{14} \text{ fm}^{-1/2}$. Although this spread appears modest, it significantly impacts the extrapolated S_{E1} . The pioneering determinations of C_1 and C_2 were made in the sub-Coulomb α -transfer experiment $^{12}\text{C}(^6\text{Li}, d)^{16}\text{O}^*$ [3], later confirmed in [4]. Both extractions relied on the input ANC $C_{\alpha d}^2 = 5.3 \pm 0.5 \text{ fm}$ from Ref. [16]. Recent *ab initio* no-core shell model with continuum calculations revised this to $C_{\alpha d}^2 = 6.864 \pm 0.210 \text{ fm}$, a $\sim 30\%$ increase, which implies a $\sim 14\%$ reduction in the deduced C_1 and C_2 values [5]. Accordingly, recommended downward renormalizations, now incorporated in Table I.

Other determinations include [6], though with larger uncertainty due to measurements above the Coulomb barrier, and model-independent extrapolation of elastic scattering [10], later confirmed by Padé extrapolation in Ref. [8]. For Bayesian inference we therefore define three priors: a flat prior on $[1.83, 2.27] \times 10^{14} \text{ fm}^{-1/2}$, a Gaussian centered at $C_1 = 1.83 \times 10^{14} \text{ fm}^{-1/2}$, and a Gaussian centered at $C_1 = 2.27 \times 10^{14} \text{ fm}^{-1/2}$.

B. ANC C_2

The situation for the subthreshold 2^+ ANC mirrors that of C_1 : the lower bound is set by [5] and the upper bound by [10]. We therefore adopt three analogous priors: a flat prior on $[0.98, 1.42] \times 10^5 \text{ fm}^{-1/2}$, a Gaussian peaked at $C_2 = 0.98 \times 10^5 \text{ fm}^{-1/2}$, and a Gaussian peaked at $C_2 = 1.42 \times 10^5 \text{ fm}^{-1/2}$.

C. ANC C_0

Ground-state ANCs reported in the literature span a wide range (see column C_0 in Table I). Earlier works favored relatively low values, while more recent determinations [11–15] suggest significantly higher values. This broad spread underscores the importance of treating C_0 consistently as part of the Bayesian framework.

III. BAYESIAN FORMALISM

A. Bayes' theorem and working space

Our goal is to infer the posterior distributions of the astrophysical factors S_{E1} and S_{E2} . Bayes' theorem for a generic parameter x reads

$$P(x | D) = \frac{\mathcal{L}(D | x) P(x)}{P(D)}, \quad (1)$$

where $P(x | D)$ is the *posterior*, i.e. the probability density of x given the data D ; $\mathcal{L}(D | x)$ is the *likelihood*, quantifying the probability of observing the data if x is assumed (see Appendix B); $P(x)$ is the *prior*, encoding information known about x before considering the new data; $P(D)$ is the normalization factor, also called the Bayesian evidence. It serves only as a normalization constant to ensure that the posterior integrates to unity: $\int P(x | D) dx = 1$. Note that both $P(D)$ and $P(C)$ are marginal probabilities: $P(D)$ is the marginal probability of the data (evidence), while $P(C)$ is the marginal probability of the parameter space (prior) (see Appendix C).

In the current scenario, the primary quantities constrained by experiment are the ANCs. The astrophysical factors S_{E1} and S_{E2} are derived observables that follow from the R -matrix mappings $S_{E1}(C_1)$ and $S_{E2}(C_2, C_0)$. Hence the posterior for S_{Ei} ($i = 1, 2$) is obtained by transforming the posterior in C through these maps.

B. ANCs as parameters

Experimental information (from transfer reactions, elastic scattering, and theoretical inputs) provides estimates \tilde{C} of the true but unknown ANCs. These measurements are typically modeled by Gaussian likelihoods,

$$P(\tilde{C} | C) \propto \exp \left[- \sum_k \frac{(\tilde{C}^{(k)} - C)^2}{2\sigma_k^2} \right], \quad (2)$$

with uncertainties σ_k . The prior distribution $P(C)$ specifies the physically allowed ANC range. In cases where no single value is preferred, we adopt a uniform prior across the interval summarized in Table I. Combining likelihood and prior yields the ANC posterior:

$$P(C | D) \propto \mathcal{L}(\tilde{C} | C) P(C). \quad (3)$$

C. Transformation to S -factors

Because S_{Ei} is not an independent parameter but a deterministic function of the ANC(s), the posterior for S_{Ei} follows by integration over C (also called variable change, propagation or push-forward):

$$P(S_{Ei} | D) = \int \delta(S_{Ei} - S_{Ei}(C)) P(C | D) dC. \quad (4)$$

The δ -function ensures that probability weight in ANC space is mapped exactly onto the corresponding values of the S -factor. Equivalently, when the mapping $S_{Ei}(C)$ is monotone on the prior support, this expression reduces to

$$P(S_{Ei} | D) = P(C(S_{Ei}) | D) \left| \frac{dS_{Ei}}{dC} \right|^{-1}, \quad (5)$$

Here $C(S_E)$ denotes the *pre-image* of S_E under the calibration map $g(C) = S_E$. In other words, for a given value of the astrophysical factor S_E , $C(S_E)$ is the ANC value that maps to it through the deterministic relation $S_E = g(C)$. Thus S_E is the image of C , while $C(S_E)$ is its corresponding pre-image.

Thus the Bayesian workflow is: (i) specify prior distributions for the ANCs, (ii) update with experimental likelihoods to obtain ANC posteriors, (iii) propagate these posteriors through the calibrated R -matrix mappings to obtain full posterior distributions for S_{E1} and S_{E2} .

D. Priors and likelihoods (single-energy treatment at 300 keV)

In Bayesian inference, a prior distribution (or simply prior) specifies the probability assigned to model parameters before incorporating the current data. It encodes existing knowledge, theoretical constraints, or assumptions, and serves as the starting point for applying Bayes'

theorem to obtain the posterior. Here we introduce priors for the three ANCs relevant at 300 keV: the subthreshold 1^- ANC C_1 , the subthreshold 2^+ ANC C_2 , and the ground-state ANC C_0 .

a. Flat priors. Our analysis of the literature values summarized in Table I indicates that C_1 is constrained to the interval $[1.83, 2.27] \times 10^{14} \text{ fm}^{-1/2}$ and C_2 to $[0.98, 1.42] \times 10^5 \text{ fm}^{-1/2}$, without preference for any subregion. Accordingly, we adopt independent uniform priors

$$p(C_1) = \mathcal{U}(1.83, 2.27) \times 10^{14} \text{ fm}^{-1/2}, \quad (6)$$

$$p(C_2) = \mathcal{U}(0.98, 1.42) \times 10^5 \text{ fm}^{-1/2}, \quad (7)$$

where $\mathcal{U}(C^l, C^h)$ denotes a uniform distribution on $[C^l, C^h]$.

b. Gaussian priors. For scenarios where specific ANC determinations are emphasized, we employ truncated normal distributions,

$$p(C) = \text{N}_T(\mu, \sigma; C^l, C^h), \quad (8)$$

with mean μ , standard deviation σ , and truncation limits C^l, C^h consistent with physical ranges. Subscript T stands for the truncation.

c. Likelihoods. At 300 keV the ANC constraints are inherited from prior determinations in the literature (Table I), rather than from new cross-section data. Each published ANC value is reported with a central estimate and uncertainty, which we represent by Gaussian likelihoods. For the $E1$ channel, the likelihood for a candidate C_1 is

$$\mathcal{L}_{E1}(D_1 | C_1) = \frac{1}{\sqrt{2\pi} \sigma_1} \exp \left[- \frac{(C_1 - \mu_1)^2}{2\sigma_1^2} \right], \quad (9)$$

where D_1 denotes the experimental determination of the subthreshold 1^- ANC, summarized by a central value μ_1 with quoted uncertainty σ_1 . In other words, $\mathcal{L}_{E1}(D_1 | C_1)$ quantifies the probability of obtaining the measured result D_1 if the true ANC were C_1 .

For the $E2$ channel,

$$\mathcal{L}_{E2}(D_2 | C_2) = \frac{1}{\sqrt{2\pi} \sigma_2} \exp \left[- \frac{(C_2 - \mu_2)^2}{2\sigma_2^2} \right]. \quad (10)$$

Here μ_i and σ_i denote the reported central values and uncertainties for each ANC. The distinction between likelihoods and priors is elaborated in Appendix B.

IV. DETERMINISTIC MAP FOR $E1$

Our Bayesian analysis relies on the R -matrix framework of Ref. [1], which provides a calibrated mapping between the ANC C_1 of the subthreshold 1^- state and the astrophysical $E1$ factor S_{E1} at 300 keV. The direct ground-state $E1$ transition is negligible, so S_{E1} depends

only on the subthreshold amplitude and its interference with the broad 1^- resonance at $E_x = 9.585$ MeV. Using the R -matrix anchors from Table VI of Ref. [1], the exact relation is

$$S_{E1}(C_1) = s_1 + \tau_1 C_1 + \beta_1 C_1^2, \quad (11)$$

with coefficients fixed by the three calibration points:

$$\begin{aligned} s_1 &= -147.23 \text{ keV b}, \\ \tau_1 &= 1.51 \times 10^{-12} \text{ keV b fm}^{1/2}, \\ \beta_1 &= -1.90 \times 10^{-27} \text{ keV b fm}. \end{aligned} \quad (12)$$

Equation (11) reproduces exactly the anchor values $S_{E1} = 65.8$ keV b at $C_1 = 1.83 \times 10^{14} \text{ fm}^{-1/2}$, $S_{E1} = 85.0$ keV b at $C_1 = 2.08 \times 10^{14} \text{ fm}^{-1/2}$, $S_{E1} = 98.0$ keV b at $C_1 = 2.27 \times 10^{14} \text{ fm}^{-1/2}$.

This quadratic calibration is used directly to transform priors on C_1 into posteriors for S_{E1} .

The mapping itself is fixed by R -matrix physics and does not depend on the choice of prior. The role of the prior is to determine how probability mass in C_1 is distributed across the map. Flat priors spread weight evenly across the full ANC range, yielding broad posteriors skewed toward higher S_{E1} due to the negative β_1 . Gaussian priors, in contrast, concentrate weight near specific ANC values (low or high anchors), producing narrower, more localized posteriors.

A. Flat prior in C_1 and analytic transformation for S_{E1}

For the current scenario we assign a uniform prior to C_1 on the accepted interval:

$$P(C_1 | D) = \frac{1}{C_1^h - C_1^l}, \quad C_1 \in [C_1^l, C_1^h]. \quad (13)$$

B. Gaussian prior in C_1 and transformation to S_{E1}

In addition to the flat prior, we also consider a Gaussian prior for the ANC C_1 , centered at an anchor value C_1^{anchor} with variance σ^2 , and truncated to the physical interval $[C_1^l, C_1^h]$:

$$P(C_1) \propto \exp\left[-\frac{(C_1 - C_1^{\text{anchor}})^2}{2\sigma^2}\right], \quad C_1 \in [C_1^l, C_1^h]. \quad (14)$$

C. Bayesian transformation and interpretation

The posterior density of S_{E1} is obtained by transforming the prior distribution of C_1 through the exact quadratic map (11).

a. Flat prior. For a flat prior, $P(C_1) = 1/(C_1^h - C_1^l)$ on $[C_1^l, C_1^h]$, the posterior is

$$\begin{aligned} P(S_{E1}) &= \frac{1}{C_1^h - C_1^l} \int_{C_1^l}^{C_1^h} \delta(S_{E1} - [s_1 + \tau_1 C_1 + \beta_1 C_1^2]) dC_1 \\ &= \frac{1}{C_1^h - C_1^l} \sum_i \frac{1}{|\tau_1 + 2\beta_1 C_1|_{C_1=C_{1,i}(S_{E1})}}, \end{aligned} \quad (15)$$

where the sum runs over real roots $C_{1,i}(S_{E1}) \in [C_1^l, C_1^h]$ of $S_{E1} = s_1 + \tau_1 C_1 + \beta_1 C_1^2$.

b. Gaussian prior. For the Gaussian prior in Eq. (14), the posterior is

$$\begin{aligned} P(S_{E1}) &= \frac{1}{Z} \int_{C_1^l}^{C_1^h} \exp\left[-\frac{(C_1 - C_1^{\text{anchor}})^2}{2\sigma^2}\right] \\ &\quad \times \delta(S_{E1} - [s_1 + \tau_1 C_1 + \beta_1 C_1^2]) dC_1 \\ &= \sum_i \frac{1}{Z} \frac{\exp\left[-\frac{(C_{1,i}(S_{E1}) - C_1^{\text{anchor}})^2}{2\sigma^2}\right]}{|\tau_1 + 2\beta_1 C_1|_{C_1=C_{1,i}(S_{E1})}}, \end{aligned} \quad (16)$$

where Z is the normalization constant ensuring $\int P(S_{E1}) dS_{E1} = 1$.

D. Interpretation of delta-function representation

The delta-function representation clarifies how probability mass in C_1 -space maps into S_{E1} -space. When the mapping $S_{E1} = g(C_1)$ is monotone, the change of variables gives

$$P(S_{E1} | D) = \frac{P(C_1(S_{E1}) | D)}{|dg/dC_1|_{C_1=C_1(S_{E1})}}, \quad (17)$$

where $C_1(S_{E1})$ denotes the preimage of S_{E1} under the map g .

The factor $P(C_1(S_{E1}) | D)$ encodes the prior weight at the corresponding ANC, while the denominator $|dg/dC_1|$ quantifies how S_{E1} responds to changes in C_1 . A steep slope ($|dg/dC_1|$ large) means that small changes in C_1 produce large changes in S_{E1} . In the change-of-variables formula the Jacobian factor $|dg/dC_1|^{-1}$ then becomes small, so the probability density is diluted over a wide range of S_{E1} values to satisfy normalization of the posterior (probability density) to unity. Conversely, a flat slope ($|dg/dC_1|$ small) implies that even large changes in C_1 produce only small variations in S_{E1} . In this case the Jacobian factor $|dg/dC_1|^{-1}$ is large, which concentrates probability weight into a narrow region of S_{E1} . Thus the shape of the posterior in S_{E1} space is controlled not only by the prior in C_1 but also by how sensitively S_{E1} responds to changes in C_1 .

For the quadratic calibration map

$$g(C_1) = s_1 + \tau_1 C_1 + \beta_1 C_1^2, \quad (18)$$

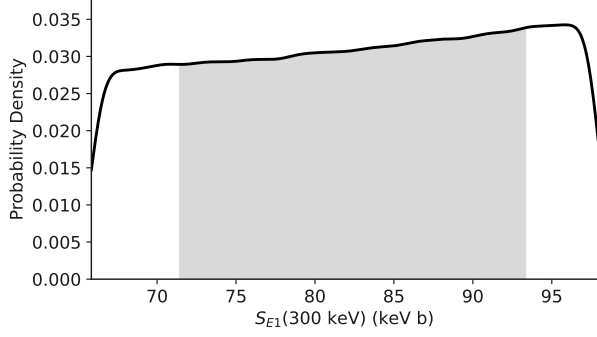


FIG. 1. Posterior of the $E1$ astrophysical factor obtained by propagating a flat prior in the ANC C_1 through the exact calibration map (11). Because the mapping is monotone with $\beta_1 < 0$, the Jacobian factor $|dS_{E1}/dC_1|^{-1}$ enhances probability density at larger C_1 , resulting in a right-skewed posterior. The grey band shows the 68% Bayesian CI.

the derivative

$$\frac{dg}{dC_1} = \tau_1 + 2\beta_1 C_1 \quad (19)$$

decreases with C_1 since $\beta_1 < 0$. Thus, the Jacobian factor $1/|dg/dC_1|$ grows toward larger C_1 , enhancing posterior density at higher S_{E1} .

Consequently, flat priors in C_1 produce right-skewed posteriors in S_{E1} . For Gaussian priors in C_1 , the outcome reflects a balance between prior weight and the Jacobian. A high-Gaussian (centered near C_1^h) produces a posterior strongly peaked at large S_{E1} , with the skew reinforced by the Jacobian. A low-Gaussian (centered near C_1^l) yields a posterior around the lower anchor, but the decreasing slope again shifts weight toward the right tail. In all cases, the right-skew of the S_{E1} posterior is a direct consequence of the concavity ($\beta_1 < 0$) of the calibration map.

Figures 1 and 2 display the posterior distributions for flat and Gaussian priors, respectively. A quantitative summary is given in Table II.

Note that for the flat prior in C_1 the posterior is strongly skewed: the MAP (see Appendix E) (~ 96 keV b) lies outside the central 68% CI because skewness displaces the posterior from the median. In skewed distributions, central CIs exclude equal tails of probability mass and need not contain the MAP.

V. POSTERIOR FOR S_{E2}

The astrophysical S_{E2} factor at $E = 300$ keV depends on two main parameters: the ANC C_2 of the subthreshold 2^+ state ($\varepsilon = 0.245$ MeV) and the ground-state ANC C_0 . We adopt the calibrated quadratic form

$$S_{E2} = s_0 + \beta_2 C_2^2 + \tau_2 C_2 C_0 + \kappa C_0^2, \quad (20)$$

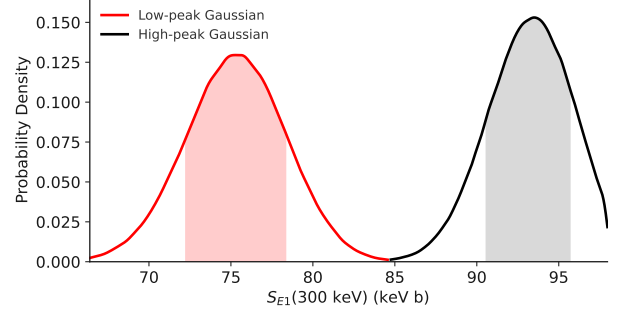


FIG. 2. Posterior distributions of the $E1$ astrophysical factor at $E = 300$ keV for Gaussian priors in C_1 . The red curve corresponds to a low-Gaussian prior centered at the $C_1 = 1.83 \times 10^{14} \text{ fm}^{-1/2}$, while the black curve corresponds to a high-Gaussian prior centered at $C_1 = 2.20 \times 10^{14} \text{ fm}^{-1/2}$. Shaded bands indicate 68% Bayesian CIs.

with S_{E2} in keV b and (C_2, C_0) in $\text{fm}^{-1/2}$. Equation (20) incorporates the capture to the ground state through the subthreshold resonance 2^+ and its interference with the direct capture to the ground state. Because the binding energy of the 2^+ state lies very close to threshold, its ANC C_2 provides the dominant contribution.

The coefficients in (20) are fixed by the four R -matrix anchors and additionally tuned to reproduce the constraint $S_{E2} = 70$ keV b at $(C_2, C_0) = (1.55 \times 10^5 \text{ fm}^{-1/2}, 337 \text{ fm}^{-1/2})$ [11]. The calibration points are: (i) at $C_0 = 58 \text{ fm}^{-1/2}$, $S_{E2} = 45$ keV b for $C_2 = 1.14 \times 10^5 \text{ fm}^{-1/2}$ and $S_{E2} = 70$ keV b for $C_2 = 1.42 \times 10^5 \text{ fm}^{-1/2}$; (ii) at $C_2 = 1.42 \times 10^5 \text{ fm}^{-1/2}$, the interference reductions yield $S_{E2} = 56.0$ keV b at $C_0 = 337 \text{ fm}^{-1/2}$ and $S_{E2} = 51.8$ keV b at $C_0 = 740 \text{ fm}^{-1/2}$. The calibrated coefficients in (20)

$$\begin{aligned} s_0 &= -0.590117303 \text{ keV b}, \\ \beta_2 &= 3.70458177 \times 10^{-9} \text{ keV b} \cdot \text{fm}, \\ \tau_2 &= -4.79813178 \times 10^{-7} \text{ keV b} \cdot \text{fm}, \\ \kappa &= 5.12789559 \times 10^{-5} \text{ keV b} \cdot \text{fm} \end{aligned} \quad (21)$$

We adopt the physically motivated prior ranges

$$C_2 \in [0.98, 1.42] \times 10^5 \text{ fm}^{-1/2}, \quad (22)$$

$$C_0 \in [58, 740] \text{ fm}^{-1/2}. \quad (23)$$

A. Prior choices

To quantify uncertainties we consider the following priors for the subthreshold and ground-state ANCs.

TABLE II. Posterior summary for S_{E1} using the exact calibrated map (11). Entries list the maximum a posteriori (MAP), the posterior median, and central 68%/95% credible intervals. Priors on C_1 are truncated to $[1.83, 2.27] \times 10^{14} \text{ fm}^{-1/2}$.

Prior on C_1	MAP (keV b)	Median (keV b)	68% CI (keV b)	95% CI (keV b)
Flat (uniform)	95.5	82.8	[71.4, 93.4]	[66.7, 97.3]
Low-Gaussian	75.4	75.3	[72.2, 78.3]	[69.2, 81.2]
High-Gaussian	93.2	93.2	[90.6, 95.7]	[87.9, 97.4]

1. C_2 priors.

Flat: $C_2 \sim \text{Unif}[0.98, 1.45] \times 10^5 \text{ fm}^{-1/2}$.
 Low- C_2 Gaussian: $C_2 \sim \mathcal{N}(1.14 \times 10^5 \text{ fm}^{-1/2}, (0.04 \times 10^5)^2)$, truncated to $[0.98, 1.45] \times 10^5 \text{ fm}^{-1/2}$.
 High- C_2 Gaussian: $C_2 \sim \mathcal{N}(1.42 \times 10^5 \text{ fm}^{-1/2}, (0.04 \times 10^5)^2)$, truncated to the same interval.

2. C_0 priors.

For the ground-state ANC we consider: Flat: $C_0 \sim \text{Unif}[58, 740] \text{ fm}^{-1/2}$.
 Fixed: $C_0 = 337 \text{ fm}^{-1/2}$ or $C_0 = 740 \text{ fm}^{-1/2}$.

B. Mixture prior for the ground-state ANC C_0

To incorporate residual uncertainty in C_0 , we also define a two-component Gaussian mixture prior reflecting the two most widely quoted determinations:

$$\pi(C_0) = w \mathcal{N}(C_0 | C_0^m, \sigma_m^2) + (1 - w) \mathcal{N}(C_0 | C_0^h, \sigma_h^2), \quad (24)$$

with $0 \leq w \leq 1$. Here $\mathcal{N}(C_0 | \mu, \sigma^2)$ is a Gaussian with mean μ and variance σ^2 . The choice $w = 1$ recovers a single Gaussian centered at $C_0^m = 337 \text{ fm}^{-1/2}$, while $w = 0$ corresponds to a Gaussian centered at $C_0^h = 740 \text{ fm}^{-1/2}$. If desired, both components can be truncated to the physical interval $[C_0^m, C_0^h]$ by replacing \mathcal{N} with truncated normal N_T distributions.

Although this mixture prior is *not* used in the current analysis (presented below with fixed or flat priors), Eq. (24) is retained for completeness. It provides a compact way to generate blended posteriors if one wishes to average over the two C_0 scenarios. Combined with the quadratic R -matrix calibration [Eq. (20)], this prior ensures that both the well-determined C_2 constraints and the residual C_0 uncertainty can be consistently propagated into the Bayesian analysis of the $E2$ transition.

C. Transformation method

The posterior distribution of S_{E2} is obtained by propagation of the joint ANC density $P(C_2, C_0 | D)$ through

the exact calibration map (20). Formally,

$$P(S_{E2} | D) = \iint \delta(S_{E2} - s_0 - \beta_2 C_2^2 - \tau_2 C_2 C_0 - \kappa C_0^2) \times P(C_2, C_0 | D) dC_2 dC_0, \quad (25)$$

where the Dirac delta ensures consistency with the deterministic map (20). In practice, this integral is evaluated by Monte Carlo sampling: pairs $(C_2^{(i)}, C_0^{(i)})$ are drawn from the priors, and the corresponding $S_{E2}^{(i)}$ values are accumulated to construct the posterior.

VI. OUTCOMES FOR S_{E2}

A. Three-dimensional S_{E2} surface

To illustrate the parameter dependence we evaluate the surface $S_{E2}(C_2, C_0)$ over the prior domains of Eqs. (22)–(23) using the exact map (20). This representation reproduces the R -matrix anchor points while remaining well behaved across the full parameter space.

Figure 3 displays the three-dimensional surface of S_{E2} evaluated on a uniform (C_2, C_0) grid, with shading corresponding to S_{E2} values in keV b. Two qualitative features are evident: (i) a steep, approximately quadratic rise with C_2 , and (ii) a moderate decrease with increasing C_0 driven by the interference term $\tau_2 C_2 C_0$.

1. Relative sensitivity to C_2 and C_0 .

the derivatives are

$$\frac{\partial S_{E2}}{\partial C_2} = 2\beta_2 C_2 + \tau_2 C_0, \quad \frac{\partial S_{E2}}{\partial C_0} = \tau_2 C_2 + 2\kappa C_0.$$

Numerically, $|\partial S_{E2}/\partial C_0|$ exceeds $|\partial S_{E2}/\partial C_2|$ locally, so per-unit variation S_{E2} is more sensitive to C_0 . However, the prior ranges differ greatly: C_2 spans $\sim 4.2 \times 10^4 \text{ fm}^{-1/2}$ and C_0 spans only $\sim 680 \text{ fm}^{-1/2}$. Consequently, varying C_2 across its interval changes S_{E2} by ~ 25 – 30 keV b , whereas varying C_0 changes it by only ~ 10 – 12 keV b . This explains why the surface in Fig. 3 is visibly steeper along the C_2 direction: although C_0 has greater local sensitivity, the much broader range of C_2 makes it the dominant driver of the overall spread in S_{E2} .

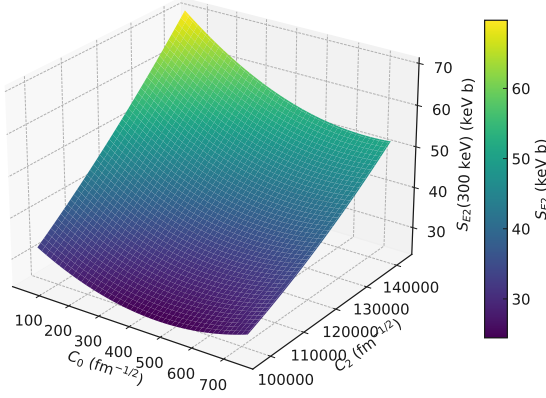


FIG. 3. Three-dimensional surface of $S_{E2}(300 \text{ keV})$ as a function of (C_2, C_0) , computed from the exact calibration (20). The dependence rises quadratically with C_2 and decreases moderately with C_0 through the interference term $\tau_2 C_2 C_0 + \kappa C_0^2$.

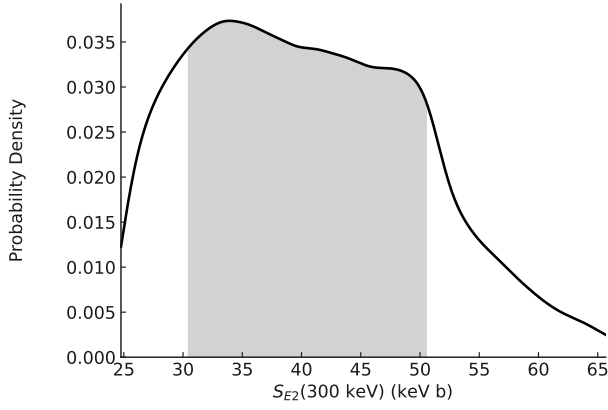


FIG. 4. Posterior of the $E2$ astrophysical factor S_{E2} obtained from the flat joint priors on $C_2 \in [0.98, 1.42] \times 10^5 \text{ fm}^{-1/2}$ and $C_0 \in [58, 740] \text{ fm}^{-1/2}$. The curve shows the Gaussian-smoothed probability density, with the grey shaded region denoting the 68% credible interval for S_{E2} : $[30.66, 50.50] \text{ keV b}$. The distribution is broad and skewed toward lower values because uniform sampling weights moderate C_2 and large C_0 values, both of which suppress S_{E2} through the quadratic terms in the exact map.

B. Posterior for joint C_2 and C_0 flat priors

The first representative posterior distribution is shown in Fig. 4.

1. Interpretation of the flat joint prior result

When both C_2 and C_0 are assigned flat priors over their physically motivated intervals, the distribution for the

TABLE III. Summary statistics for $S_{E2}(300 \text{ keV})$ under flat joint prior. Entries give MAP, median, and central 68% Bayesian credible interval.

MAP (keV b)	Median (keV b)	68% CI (keV b)
33.91	40.06	[30.66, 50.50]

astrophysical factor S_{E2} is shifted toward relatively low values compared to scenarios with Gaussian constraints. This behavior can be understood from two compounding effects.

First, S_{E2} rises approximately as C_2^2 . Under a flat prior on $C_2 \in [0.98, 1.42] \times 10^5 \text{ fm}^{-1/2}$, the sampling places equal weight across the interval, so moderate values of C_2 dominate. Since high C_2 values drive large S_{E2} , the lack of bias toward the upper end shifts probability toward lower S_{E2} values.

Second, the terms $\tau_2 C_2 C_0$ and κC_0^2 introduce an additional suppression with increasing C_0 . With a flat prior on $C_0 \in [58 - 740] \text{ fm}^{-1/2}$, a substantial fraction of samples fall at large C_0 values, where these terms reduce S_{E2} .

The joint flat prior therefore combines two tendencies: (i) equal weight across C_2 , which down-weights the high- C_2 values most responsible for large S_{E2} , and (ii) equal weight across C_0 , which enhances the contribution of the suppressive terms. The resulting posterior is broad and left-skewed, with MAP and median values shifted to lower keV b compared to the Gaussian-constrained cases.

C. Posterior distributions for $S_{E2}(300 \text{ keV})$ at fixed C_0

Figure 5 shows the posterior densities of the $E2$ astrophysical factor at $E = 300 \text{ keV}$ for two representative ground-state ANC, $C_0 = 337 \text{ fm}^{-1/2}$ and $C_0 = 740 \text{ fm}^{-1/2}$. In each case, two scenarios are displayed, corresponding to Gaussian priors on the subthreshold 2^+ ANC C_2 centered at the low- and high-anchor values (both truncated to the physical interval). The densities are obtained by propagating $P(C_2, C_0 | D)$ through the exact calibration map (20) and smoothed using a Gaussian kernel (see Appendix F). The lower- S_{E2} mode (low- C_2 prior) is shown in red with red 68% CI shading, while the higher- S_{E2} mode (high- C_2 prior) is shown in black with grey shading. The separation between the two modes reflects the quadratic dependence $S_{E2} \propto C_2^2$, while the downward shift from $C_0 = 337$ to $C_0 = 740$ quantifies the suppression from the interference terms $\tau_2 C_2 C_0$ and κC_0^2 .

The main features are:

High- C_2 priors yield posterior peaks $\sim 50 - 60\%$ larger than the low- C_2 case.

The C_0 effect is weaker but non-negligible, lowering S_{E2} by $\sim 7 - 8\%$ when C_0 increases from $337 \text{ fm}^{-1/2}$ to $740 \text{ fm}^{-1/2}$.

TABLE IV. Summary statistics for $S_{E2}(300 \text{ keV})$. Entries give MAP, median, and central 68%/95% Bayesian credible intervals for each (C_0, C_2) case.

$C_0 \text{ (fm}^{-1/2}\text{)}$	$C_2 \text{ (fm}^{-1/2}\text{)}$	MAP (keV b)	Median (keV b)	68% CI (keV b)	95% CI (keV b)
$C_0 = 337$	low C_2	42.06	41.92	[40.73, 43.12]	[39.57, 44.28]
$C_0 = 337$	high C_2	53.67	53.52	[52.23, 54.82]	[50.98, 56.07]
$C_0 = 740$	low C_2	38.74	38.62	[37.53, 39.72]	[36.47, 40.78]
$C_0 = 740$	high C_2	49.45	49.42	[48.23, 50.62]	[47.07, 51.78]

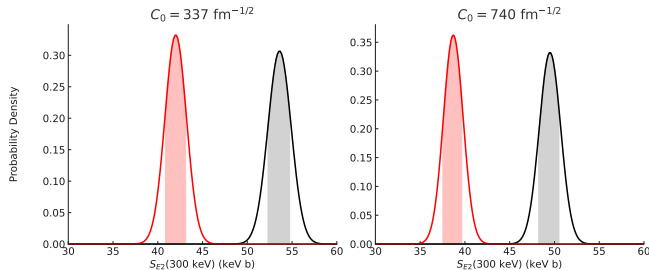


FIG. 5. Posterior densities of $S_{E2}(300 \text{ keV})$ under Gaussian priors on C_2 , shown for $C_0 = 337 \text{ fm}^{-1/2}$ (left) and $C_0 = 740 \text{ fm}^{-1/2}$ (right). The low- C_2 Gaussian centered at $C_2 = 1.14 \times 10^5 \text{ fm}^{-1/2}$ gives the lower- S_{E2} mode (red curve, red shading). The high- C_2 Gaussian centered at $C_2 = 1.42 \times 10^5 \text{ fm}^{-1/2}$ gives the higher- S_{E2} mode (black curve, grey shading). At fixed C_0 , the separation between red and black modes reflects the quadratic C_2 dependence, while the overall downward shift from $C_0 = 337 \text{ fm}^{-1/2}$ to $C_0 = 740 \text{ fm}^{-1/2}$ arises from destructive interference with the ground-state channel.

D. Discussion

The results show that S_{E1} is highly sensitive to the assumed value of the 1^- ANC C_1 , with the quadratic dependence leading to sizable shifts between the low- and high-anchor priors. By contrast, S_{E2} is primarily controlled by the subthreshold 2^+ ANC C_2 , while interference with the ground state through C_0 induces an additional reduction whose magnitude grows with C_0 . The observed downward shift of S_{E2} with increasing C_0 is therefore a robust signature of destructive interference between the 2^+ subthreshold amplitude and the direct ground-state capture.

Together, these posteriors quantify the uncertainties in the extrapolated S -factors for the $^{12}\text{C}(\alpha, \gamma)^{16}\text{O}$ reaction at $E = 300 \text{ keV}$. The dominant sources of uncertainty are the subthreshold ANCs C_1 and C_2 , with a secondary contribution from the ground-state ANC C_0 . Using the most reliable contemporary ANC constraints, we find that under flat priors the 68% credible intervals are

$$\begin{aligned} S_{E1} &\in [71.4, 93.4] \text{ keV b}, \\ S_{E2} &\in [30.7, 50.5] \text{ keV b}. \end{aligned} \quad (26)$$

These intervals encapsulate the present theoretical and experimental uncertainties and provide statistically ro-

bust ranges for stellar modeling applications.

VII. ACKNOWLEDGMENTS

The author thanks Alex Zhanov for technical assistance. The author also would like to acknowledge the assistance of AI (Open AI's ChatGPT5) for editorial and formatting support during the preparation of the manuscript. All scientific results, interpretations and conclusions are solely those of the author.

Appendix A: Marginal versus conditional probabilities

In Bayesian inference it is important to distinguish between marginal and conditional probability densities:

- **Conditional probability density:** Describes the distribution of one parameter given that another is fixed. For example, $P(S | C)$ denotes the distribution of the S -factor when the ANC C is assumed to have a specific value.
- **Marginal probability density:** Obtained by integrating (“summing over”) other variables, thereby removing them. For example,

$$P(S) = \int P(S | C) P(C) dC \quad (\text{A1})$$

is the marginal density of the S -factor, averaged over all possible C values weighted by their prior or posterior density.

In short:

Conditional: distribution of one parameter given a fixed value of another (e.g. $P(S | C)$).

Marginal: distribution after integrating out the uncertainty in the other variables (e.g. $P(S) = \int P(S | C) P(C) dC$).

Appendix B: Likelihood versus probability

It is also crucial to separate the concepts of probability and likelihood:

- **Probability (density):** Quantifies how likely a future or hypothetical observation is, given a fixed model and parameters. For example,

$$P(D | C) \quad (\text{B1})$$

is the normalized probability of observing the data D if the ANC C has a particular value.

- **Likelihood:** The same expression viewed as a function of the parameter with data D fixed:

$$\mathcal{L}(C | D) \propto P(D | C). \quad (\text{B2})$$

The likelihood is not normalized in C , but it provides the relative weight of different candidate values given the observed data.

In short: probability treats the parameter as fixed and the data as variable, while likelihood treats the data as fixed and the parameter as variable.

For example, the probability density of the data \tilde{C} given the ANC C is modeled by a Gaussian,

$$P(D | C) \propto \exp \left[-\frac{(\tilde{C} - C)^2}{2\sigma^2} \right]. \quad (\text{B3})$$

Viewed as a function of C , this expression is the *likelihood*,

$$\mathcal{L}(C | D) \propto \exp \left[-\frac{(\tilde{C} - C)^2}{2\sigma^2} \right]. \quad (\text{B4})$$

The symbol “ \propto ” indicates proportionality: the right-hand side gives the shape of the function in C , while the omitted normalization constant ensures that $P(D | C)$ integrates to one over all possible data. In Bayesian inference, this normalization is irrelevant because D is fixed (the data have already been observed). What matters is the relative weight of different C values, which is fully specified by the likelihood.

Appendix C: Marginal probabilities

In Bayesian inference two types of marginal probabilities appear naturally.

- **Evidence as a marginal over parameters.** The normalization factor in Bayes’ theorem,

$$P(D) = \int P(D | C) P(C) dC, \quad (\text{C1})$$

is the marginal probability of the data D , obtained by integrating over all possible parameter values C . This quantity, also called the *evidence*, ensures that the posterior $P(C | D)$ is normalized.

- **Prior as a marginal over nuisance parameters.** When a model involves several parameters, e.g. (C_0, C_1, C_2) , one often specifies a joint prior $P(C_0, C_1, C_2)$. The prior for a single parameter, say C_1 , is then obtained by integration:

$$P(C_1) = \iint P(C_0, C_1, C_2) dC_0 dC_2. \quad (\text{C2})$$

Thus $P(C)$ in Bayes’ theorem is itself a marginal probability distribution defined before the data are taken into account.

In summary, $P(D)$ is a marginal probability in *data space*, while $P(C)$ is a marginal probability in *parameter space*.

Appendix D: Credible intervals.

In Bayesian inference, two types of credible intervals (CIs) are commonly reported:

- **Central (CIs):** defined as symmetric in probability mass around the posterior median. That is, equal probability is excluded from both tails of the distribution (e.g. 16% from each tail for a 68% central CI). Note that for skewed posteriors, the resulting interval is not symmetric in the parameter axis and may not contain the MAP.
- **Highest posterior density intervals (HPDIs):** defined as the shortest interval(s) containing the specified probability mass. HPDIs always include the MAP and can be asymmetric.

The reported intervals in this work are the central CIs.

Appendix E: MAP, median, and mean.

The MAP (maximum a posteriori) is the point of highest probability density. The *median* is the value that divides the posterior into two equal probability halves. The *mean* is the expectation value, obtained by averaging the posterior. For symmetric posteriors all three coincide, but for skewed posteriors they generally differ.

Appendix F: Kernel density estimation (KDE)

When computing posteriors for S_{E1} and S_{E2} , we generate large Monte Carlo samples from the ANC distributions and map them through the R -matrix formulas. A raw histogram of these samples would appear noisy and bin-size dependent. To provide smooth curves we use *kernel density estimation* (KDE).

In KDE, each sample point is replaced by a small Gaussian “bump.” Adding all these bumps produces a smooth

approximation to the underlying density:

$$\hat{p}(x) = \frac{1}{Nh} \sum_{i=1}^N K\left(\frac{x - x_i}{h}\right),$$

where K is the Gaussian kernel and h is the bandwidth.

In our figures KDE is used purely for visualization. The shaded 68% bands are computed directly from the Monte Carlo samples, while the KDE curves guide the eye by showing the posterior shape more clearly.

-
- [1] A. M. Mukhamedzhanov, Phys. Rev. C **110**, 055803 (2024).
 - [2] D. Odell *et al.*, Frontiers in Phys. **10**, 888476 (2022).
 - [3] C. R. Brune, W. H. Geist, R. W. Kavanagh, and K. D. Veal, Phys. Rev. Lett. **83**, 4025 (1999).
 - [4] M. L. Avila *et al.*, Phys. Rev. Lett. **114**, 071101 (2015).
 - [5] C. Hebborn *et al.*, Phys. Rev. C **109**, L061601 (2024).
 - [6] A. Belhout *et al.*, Nucl. Phys. A **793**, 178 (2007).
 - [7] N. Oulevsir *et al.*, Phys. Rev. C **85**, 035804 (2012).
 - [8] O. L. Ramírez Suárez and J.-M. Sparenberg, Phys. Rev. C **96**, 034601 (2017).
 - [9] R. J. deBoer *et al.*, Rev. Mod. Phys. **89**, 035007 (2017).
 - [10] L. D. Blokhintsev, A. S. Kadyrov, A. M. Mukhamedzhanov, and D. A. Savin, Eur. Phys. J. A **59**, 162 (2023).
 - [11] Y. Shen *et al.*, Astrophys. J. **945**, 41 (2023).
 - [12] D. B. Sayre, C. R. Brune, D. E. Carter *et al.* 2012, Phys. Rev. Lett. **109**, 142501 (2012).
 - [13] L. H. Chien and P. Descouvemont, Phys. Rev. C **110**, 024611 (2024).
 - [14] S. Adhikari *et al.*, J. Phys. G **44**, 015102 (2017).
 - [15] K. Kundalia *et al.* Phys. Lett. B, 139836 (2025), accepted for publication
 - [16] L. D. Blokhintsev, V. I. Kukulin, A. A. Sakharuk, D. A. Savin, and E. V. Kuznetsova, Phys. Rev. C **48**, 2390 (1993).